Inner-shell photodetachment from Ni^{−}: A giant Feshbach resonance

I. Dumitriu, R. C. Bilodeau, T. W. Gorczyca, C. W. Walter, N. D. Gibson, D. Rolles, Z. D. Pešić, A. Aguilar, and N. Berrah

Phys. Rev. A **96**, 023405 — Published 2 August 2017

DOI: 10.1103/PhysRevA.96.023405

Inner-Shell Photodetachment from Ni^-: Giant Feshbach Resonance

I. Dumitriu [a], R. C. Bilodeau [b, c], T. W. Gorczyca [d], C. W. Walter [e], N. D. Gibson [e], D. Rolles [f], Z. D. Pešić [c, †], A. Aguilar [c],[‡] and N. Berrah [b]

[a] Department of Physics, Hobart and William Smith Colleges, Geneva, NY 14456
[b] Department of Physics, University of Connecticut, Storrs, CT 06269
[c] Advanced Light Source, Lawrence Berkeley National Laboratory, Berkeley, CA 94720
[d] Department of Physics, Western Michigan University, Kalamazoo, MI 49008
[e] Department of Physics and Astronomy, Denison University, Granville, OH 43023
[f] J. R. Macdonald Laboratory, Department of Physics, Kansas State University, Manhattan, KS 66506

Abstract

Inner-shell photodetachment from Ni^-([Ar] $3d^9 4s^2$) leading to Ni^+, Ni^{2+}, and Ni^{3+} ion production was studied near and above the 3*p* excitation region, in the 60 - 90 eV photon energy range, using a merged ion-photon beam technique. The absolute photodetachment cross section of Ni^- leading to Ni^+ ion production was measured. The $3p \rightarrow 3d$ photoexcitation in Ni^- gives rise to a giant Feshbach resonance. In the near-threshold region, a Fano profile, modified by a Wigner *s*-wave (l=0) threshold law, accurately fits the Ni^- single photodetachment cross section. A lower-order R-matrix calculation shows overall agreement with essential features of the experimental data, confirming the nature of the strong, asymmetric Fano profile of the giant $3p \rightarrow 3d$ photoexcitation-autodetachment resonance in Ni^-.

[†] present address: ThermoFisher Scientific, East Grinstead, UK

[‡] present address: ReVera Inc., Santa Clara, CA

1. Introduction

Negative ions play an important role in various branches of physics, ranging from astrophysics, atmospheric and plasma physics, to surface and accelerator physics. Due to the excess of negative charge compared to the neutral parents, negative ions show enhanced correlation effects. Therefore negative ions are well suited theoretical test objects within atomic physics, and investigation of the dynamics of negative ions yield insights into many-body effects and understanding of electronic structure [1].

The lowest order single photodetachment process of a negative ion involves the detachment of a single electron following the absorption of a single photon, $h\nu + A^- \rightarrow A + e^-$. In the case of the inner-shell photodetachment, the remaining neutral atom will be in an excited state that, mostly likely, will subsequently Auger decay resulting in a positive ion. Photodetachment of negative ions differs fundamentally from photoionization of neutral atoms and positive ions due to the nature of the force binding the outermost electron. In a negative ion the outermost electron experiences a shorter-range field arising from the polarization of the atomic core. In an atom or positive ion, the outer electron moves in the long-range Coulomb field of the positive charged nucleus shielded by the inner electrons. The long-range Coulomb field is able to support an infinite spectrum of bound states, whereas the short-range field in negative ions is much shallower and can typically support only a single bound state. Only in rare cases (for example, in Ce^- [2], La^- [3], Os^- [4], Pt^- and Ir^- [5, 6]) are there any bound excited states with a different configuration than the ground state. However, negative ions possess excited states lying above the detachment limit, embedded in the continuum associated with the free electron and the neutral atom.

Feshbach resonances result from an excitation that lies *below* its neutral parent state and, thus cannot decay into the parent state; instead, they decay to lower-lying states of the atom via simultaneous de-excitation of one electron and ejection of another [7]. Feshbach resonances due to stabilization of the *p* valence orbital were previously observed with $1s \rightarrow 2p$ excitation in He^- [8], $2s \rightarrow 3p$ excitation in S^- [9], and $4d \rightarrow 5p$ excitation in Te^- [10].

Shape resonances are situated just *above* their parent atomic state. In this case, the one-electron potential produced by the short-range attraction and the centrifugal repulsion forms a barrier large enough to trap the electron inside it. The decay mechanism is tunneling through the barrier [7], and the resonances are consequently broad structures in the photodetachment cross section. Since they are often located very close to a threshold, the corresponding Wigner threshold behavior is severely altered by their presence as pointed out by Peterson *et al*. [11, 12]. Such shape resonances have been reported in other inner-shell photodetachment studies such as in Li^- [13, 14, 15, 16], B^- [17, 18, 19], C^- [20, 21, 22], Fe^- [23] and Ru^- [24]. Both types of resonances were observed in the Pt^- ion [25].

The interplay of the attractive and repulsive interactions in a negative ion is of fundamental interest and allows us a better understanding of correlated systems such as certain nanostructures, superconductor materials, and magnetic thin films for modern data storage technology [26]. Industry is interested in probing the atomic limits since the magnetic properties do not scale linearly with the number of atoms in a sample. While in applications, mostly bulk material is used, atomic species are of great interest for research, too. In order to gain a simple picture of the bulk properties, data on single atoms

is valuable. More than that, investigating atoms in the gas phase comes with the advantage of high resolution and without the complicated solid state effects. The *d*-orbital retains, to a high degree, the same characteristics in solids [26, 27, 28], so the atomic and ionic data could be very useful to contribute information toward understanding intra- and inter-atomic effects.

Transition metals such as nickel are particularly interesting to study spectroscopically with bright, monochromatized radiation available from synchrotron light sources. Atomic nickel is a difficult sample to prepare in the gas phase due to high temperature required to vaporize the metal [29]. Despite experimental difficulties, the electronic structure and correlation effects in free nickel atoms were studied by resonant Auger spectroscopy [30, 31], and the $M_{2,3}$-shell Auger and autoionisation spectra of free Ni atoms were also investigated [32]. The 3*p* photoelectron spectrum [33] and the 2*p* spectrum [34] of atomic Ni have been measured by using synchrotron radiation and atomic beam techniques. A resonant enhancement of the vacuum ultraviolet photoemission lines above the 3*p* threshold was observed in atomic Fe, Co, and Ni [35]. Later, the 3*p*-photoionization resonances for Ni atoms in the region of 30 – 80 eV were studied by detecting the singly- and doubly-charged photoions using the time-of-flight method [36]. Verweyen *et al*. [37] used an ultraviolet-laser to prepare a beam of free Cu atoms in a "Ni –like" state and investigated the emission of 3*d* electrons. Absolute measurements of the photoionization cross section for Ni^+ positive ions in the 50 - 80 eV photon energy range were reported [38].

The negative ion of nickel was previously studied by valence-shell laser photodetachment spectroscopy to measure the fine structure splitting and the binding

energy of the Ni^- ground state (1.15716(12) eV, the electron affinity of Ni) [39]. The electron affinities for the lowest 3 excited configurations in Ni^- have been calculated [40]. The lifetime (15.1 ± 0.4 s) of the Ni^- excited bound level, decaying to the ground states via the $3d^9 4s^2\ ^2D_{3/2} \rightarrow 3d^9 4s^2\ ^2D_{5/2}$ radiative transition, has been measured in an ion-beam storage ring experiment [41].

A strong feature in the cross section, the so-called "giant resonance", has been observed in the core-level photoionization spectra of atomic 3*d* transition metals [26]. It is therefore of interest to determine whether or not a similar "giant" resonance is also present in the photodetachment cross section of the Ni^- atomic negative ion. Absolute photodetachment cross sections are extremely important to know in order to interpret the soft X-ray spectra of many astronomical objects, such as galactic nuclei and X-ray binary systems [42]. For negative ions, the absolute photodetachment cross section measurements are very challenging due to low ion-target density, low signal and high background. Therefore, experimental data on the photodetachment cross section of negative ions are very limited compared to the cross section data on neutral atoms and positive ions.

In this study, we measured the absolute cross section for the production of Ni^+ and the ratio of channel strengths (Ni^{2+}/Ni^+) and (Ni^{3+}/Ni^+) at four photon energies. The aim of this work is to provide reference data for astrophysics and plasma physics, and a testing ground for the ability of theoretical methods to model correlation processes. The experimental results show good qualitative agreement with single photodetachment cross sections of Ni^- obtained from a lower-order (minimal configuration, non-relativistic) R-matrix calculation. Evidence of a giant resonance is observed in both experiment and

theory, as seen as a broad asymmetric profile arising from interference between the direct $3d \rightarrow \varepsilon f$ continuum $3d$ and $4s$ photodetachment and the indirect (resonant) $3p$-$3d$ photoexcitation followed by autodetachment.

2. Experimental Method

The experiment was performed at the Advanced Light Source (ALS), Lawrence Berkeley National Laboratory, using the High Resolution Atomic Molecular and Optical Physics (HRAMO) undulator beamline 10.0.1 with the ion-photon beamline (IPB). The IPB endstation [43] uses the merged beam technique for photoion spectroscopy, where ions and photons travel collinearly in order to increase the interaction volume between photons and the dilute ion beam, see Figure 1.

The ions were accelerated to 7.5 keV in a cesium sputter source (SNICS II from NEC) [44], focused by an Einzel lens and deflected by an analyzing magnet to select the charged ion of interest, Ni^{-}. The ion beam is merged onto the axis of the counter-propagating photon beam by a pair of 90º spherical-sector bending plates. A hole in the back plate of the merger allows the photon beam to pass through and be detected by a calibrated silicon photodiode.

The intensity distribution of both beams is measured by rotating-wire beam profile monitors installed upstream and downstream of the interaction region. The overlap between the ion and photon beam is monitored by three translating slit-scanners, located near the entrance, middle, and exit of the interaction region. The monitors are removed from the beam path during data collection.

The products resulting from the photodetachment process (positive ions) are separated from the parent beam (negative ions) by an analyzing magnet "demerger" located downstream of the interaction region. The positive ions (signal) are directed onto a stainless steel plate biased at –550 V by a spherical 90º electrostatic deflector. Secondary electrons emitted by the steel plate are accelerated and detected by a channel electron multiplier detector used in a pulse-counting mode.

In this experiment, ion currents of 350 nA were recorded after shaping and spatial trimming of the Ni negative ion beam. The inner-shell photodetachment and subsequent Auger decay produce positive ions that were deflected by the demerger magnet and counted as a function of photon energy. The photon-ion interaction region was defined by a 29.4 cm long stainless-steel cylinder. The 7.5 keV incoming ions were kinetic energy tagged by applying a constant potential of +0.75 kV to the interaction region. The Ni^- ions entering in the interaction region were thus accelerated to 8.25 keV, and the positively charged ions Ni^+ (Ni^{2+}) resulting from the photodetachment process exited the interaction region experiencing a second kinetic energy boost of +0.75 keV (+1.50 keV), leaving with 9 keV (9.75 keV) of kinetic energy. The Ni^+ and Ni^{2+} ions formed outside of the interaction region, having a lower kinetic energy of 7.5 keV, could then be selected against by the demerger magnet and spherical electrostatic deflector located before the detector.

The positive ions produced by stripping collisions of the primary ion beam with the residual gas or apertures in the interaction region, are also detected and counted together with the photoions. The background count rate of these ions is not negligible even under the ultra-high vacuum conditions (≈4 x 10^{-10} Torr in the interaction region)

and so the photon beam is chopped at a frequency of 6 Hz. By chopping the photon beam and subtracting the "photon-off" from the "photon-on" counts, the background signal is accounted for, and the photodetachment signal is obtained.

As shown in Figure 2, the ground state energies of Ni, Ni^+, Ni^{2+}, and Ni^{3+}, relative to the Ni^- ground state, are, respectively, 1.15716(12) eV [39], 8.797037(121) eV [45], 26.965874(123) eV [46], and 62.153(19) eV [47] [uncertainties are quoted to 1 standard deviation (SD) throughout]. Ni^{4+} (117.07(26) eV [46, 48]) and higher charged state products are therefore not energetically possible to produce with the photon energies, 60 – 90 eV, used in the present experiment. All three energetically allowed ionic products were measured. Note that only charged products can be detected with the present apparatus and any neutral Ni produced could not be detected.

The photon energy was scanned, the incident photon flux was recorded by an absolutely calibrated silicon X-ray photodiode, and the ion current was monitored with a Faraday cup placed after the de-merging magnet. The resulting photodetachment signal was normalized to the incident photon flux and the negative ion current. Several sweeps over the photon energy of interest were recorded and summed in order to improve the signal-to-noise ratio. The photon energy scale was calibrated using accurately known (2 to 4 meV) absorption lines in He [50]. The total uncertainty in the calibrated lab-frame photon energy was estimated to be 25 meV @ 46 eV, 15 meV @ 60 eV, 25 meV @ 75 eV and 80 meV @ 90 eV photon energy. By the direct measurement of the interaction bias potential and the ion source acceleration potentials, the beam energy in the interaction region was determined to be 8.25(30) keV which gives sufficient ion velocity

to produce a significant Doppler shift, and an energy correction to account for this Doppler shift has been applied to all the spectra reported here.

For negative ions generated by a sputter source, the temperature of the sputter area gives rise to a Boltzmann population of the ionic states. The relative intensities of the Ni^- thresholds for populations resulting from a 'cool' (T= 650 K) and 'hot' (T=1300 K) sputter source were previously reported [39] showing that for a 'cool' source, there is a negligible (less than 2%) contribution of the excited states in the photodetachment cross section. In this experiment, the negative ion source was operated at a relatively low temperature (< 700 K) and therefore, we expect that only the $^2D_{5/2}$ ground-state level of Ni^- was populated significantly.

3. Results and Discussion

A. Measured Photodetachment Spectra

The absolute cross sections for photoexcitation of Ni^- leading to Ni^+ production were measured for the four photon energy points listed in Table I. The absolute cross sections (σ) are calculated from the measurements of the target-ion current (I), velocity of the negative ions (v), charge of the negative ions (q), signal rate (R), form factor (F), and photon flux (Φ) as follows: $\sigma = (q\ v\ R) / (I\ \Phi\ F)$ [43]. The signal rate is $R = R_0 / \Omega_{det}$, where R_0 is the measured count rate, and Ω_{det} is the detector efficiency. In the present experiment, the detector efficiency Ω_{det} was estimated to be 0.95(10). The total (one standard deviation) systematic instrumental error was 25 %.

The two dimensional form factors, $F_z = \int i_x \Phi_x dx \int i_y \Phi_y dy$, were estimated based on the ion (i) and photon (Φ) beam profiles which are measured by the slit scanners. The total form factor (F), a measure of the quality of the overlap of the ion beam with the photon beam, is obtained by integration of the quadratic interpolation of these three 2D form factors over the interaction region length. For an accurate determination of the form factor, the ion-photon interaction volume must be well defined [43]. This was accomplished with the +0.750(15) kV voltage applied to the interaction region. The effective interaction region length of 28.3(14) cm was determined from electrostatic simulations using SIMION 7.00 [51] and the ion kinetic energy acceptance of the spherical-sector deflectors positioned just before the positive-ion detector.

The ratio of channel strengths (Ni^{2+}/Ni^{+}) and (Ni^{3+}/Ni^{+}) was measured at the same photon energies as the absolute cross sections following the same procedure as previous experiments [9, 23, 24, 52]. With the present apparatus, only one channel can be monitored at any particular time. So, the signal rates $R(Ni^{+})$, $R(Ni^{2+})$, and $R(Ni^{3+})$ were recorded in rapid succession (1- 4 min per product per energy point) and the measurements were repeated five times to verify that no significant fluctuations in the overlap, ion current, or other such effects were present. The ratio of channel strengths (Ni^{2+}/Ni^{+}) and (Ni^{3+}/Ni^{+}) are reported in Table I.

The very weak signal observed in the Ni^{2+} and Ni^{3+} channels made direct absolute cross section measurements prohibitive. Instead, the ratio of channel strengths from Table I were used in combination with Ni^{+} absolute cross section measurements to obtain estimates of $\sigma(Ni^{2+})$ and $\sigma(Ni^{3+})$. Figure 3 shows the absolute photodetachment cross section of Ni^{-} to the Ni^{+}, Ni^{2+}, and Ni^{3+} product channels. The circles with error bars in

Figure 3 represent the absolute cross section measurements to which the spectra are normalized by using the same method as in previous experiments [9, 23, 24, 52]. Production of Ni^{3+} is possible only above the 4-electron threshold at 62.153(19) [47], and most likely involves highly correlated many-electron processes over the photon energy range scanned in this experiment, 60 – 90 eV. Also, no distinction can be made between the different excited states of the detected Ni^{+}, Ni^{2+}, and Ni^{3+} ions and, thus, the data shown in Figure 3 represent the sum of all the partial cross sections.

Photodetachment of Ni^{-} ([Ar] $3d^9 4s^2\ ^2D_{5/2}$) proceeds from the inner $3p$ shell at photon energies higher than 65 eV. In the neutral Ni atom, the binding energies of the inner-shell $3p$ electrons are 66.2 eV ($3p_{3/2}$) and 68 eV ($3p_{1/2}$) [53]. The relevant states in the negative ion, the parent Ni atom, and the Ni^{+}, Ni_2^{+}, Ni^{3+} positive ions are presented in Figure 2.

Figure 3 shows the signal observed in the Ni^{+}, Ni^{2+}, and Ni^{3+} product channels following $3p$ photodetachment and excitation of Ni^{-}. In the $Ni^{-} \rightarrow Ni^{+}$ photodetachment cross section, there is a dip below 65 eV, followed by a sharp increase in the cross section near the $3p$ threshold. In contrast, in the Ni^{2+} channel the signal is monotonically increasing, no dip is observed, and there is about ten times less background. The signal in the Ni^{3+} channel shows similar behavior to the Ni^{+} signal but has a much smaller cross section (~ 0.003 Mb). The most significant feature of Figure 3 is a resonance observed in all three channels around 65 eV, which is likely due to $3p \rightarrow 3d$ excitation. Above 68 eV, the Ni^{+} production continues to decreases monotonically while that of Ni^{2+} instead increases indicating some new channel may be opening for Ni^{2+} production, but is blind to Ni^{+} production. For the photodetachment of the Ni^{-}negative ion, the ratio Ni^{2+}/Ni^{+}

rises from 0.130 ± 0.010 at 60 eV to 0.280 ± 0.019 at 89 eV. For the photoionization of the Ni atoms, ratio of Ni^{2+}/Ni^{+} slowly rises from a value of 0.15 ± 0.03 at 68 eV to 0.58 ± 0.04 at 80 eV [36]. Similar behavior was observed for photoionization of Co, and Fe atoms [36] and for photodetachment of Fe^{-} [23]. A broad feature is observed near 70 eV in the Ni^{+} channel and is not readily seen in the other channels.

B. Theoretical Calculations

In order to gain a qualitative understanding of the resonance phenomena occurring in the complete Ni^{-} inner-shell photodetachment process, we performed lower-order calculations using the R-matrix method [54, 55]. In this study, we follow the basic theoretical methodology used for R-matrix calculations for Li^{-} [13], B^{-} [17, 18], C^{-} [20, 21], Fe^{-} [23], and Ru^{-} [24], and seek a minimal configuration and orbital basis for capturing the essential physics. For the present Ni^{-} photodetachment case, we first included all symmetries consistent with the photodetachment process at hand: $Ni^{-}(3p^{6}3d^{9}4s^{2}) \rightarrow Ni(3p^{6}3d^{8}4s^{2})$.

Thus we included an initial bound state of ^{2}D even symmetry for the $3p^{6}3d^{9}4s^{2}$ Ni^{-} state, spanned by a basis of all configurations $3p^{a}3d^{b}4s^{c}$ (a+b+c=17), and all ^{2}P, ^{2}D, and ^{2}F final detachment symmetries, spanned by a basis of configurations $3p^{a}3d^{b}4s^{c}$ (a+b+c=16) for the final Ni states, coupled to outgoing Coulomb waves for the photodetached electron. The minimal orbital basis (1s, 2s, 2p, 3s, 3p, 3d, and 4s) was optimized for the $3p^{-1}$ inner-shell vacancy states. This limited basis set thus fails to represent completely the photodetachment continua for the filled 3p Ni states, resulting in *relaxation* inaccuracies in the final wavefunction and photodetachment cross section.

Nevertheless, the important 3*p*-3*d* photoexcited giant resonance is represented by an optimal orbital set.

Nickel is considered a prototype system in the 3*d* transition metal series regarding strong correlations and configuration interactions in the ground, core-, and valence-excited states. Whereas an enormous amount of configuration interaction and a large number of neutral Ni target states would be needed to obtain any type of converged atomic description, and relativistic effects are certainly non-negligible, we were only concerned with the gross features of the photodetachment process, so the problem was simplified as follows. First, all relativistic effects, including the spin-orbit interaction, were omitted so that an LS description was valid. Second, our atomic basis consisted of a minimal-configuration description for the initial Ni^- ([Ar] $3d^9 4s^2\ ^2D_{5/2}$) ground state, the photodetached neutral Ni ([Ar] $3d^8 4s^2\ ^3F_4$) ground state, and 16 of the 3*p*-excited Ni* final target states, as listed in Table II.

The total absolute cross section for $Ni^- + h\nu \rightarrow Ni^* + e^-$ photodetachment was calculated in both length and velocity gauge (see Figure 4). Since we were not concerned with the outer-shell photodetachment process, we chose an orbital basis specific to $3p^{-1}$ vacancy states; consequently, the 3*d* and 4*s* outer-shell photodetachment processes that comprise the signal below the inner-shell threshold, are described using orbitals that are not optimal for these filled-3*p*-states of Ni. Indeed, these limited R-matrix calculations produce photodetachment cross sections that differ by a factor of two depending on whether the length or velocity form of the dipole operator is used. For an exact wavefunction, the analytical cross sections in both gauges are equivalent, so a factor of two difference indicates an inaccuracy in the photodetached wavefunction. Nevertheless,

the shape, asymmetry, and strength of the giant resonance is essentially the same in both length and velocity gauges – only the background outer-shell photodetachment cross sections differ – and therefore, either calculation is sufficient for further theoretical analysis. As is well known, the computed length-gauge cross section emphasizes the long-range nature of the wavefunctions whereas the velocity-gauge result depends more on the inner region. Since we are considering *inner-shell* 3*p* photodetachment involving transitions near the atomic core, we choose to continue with velocity-gauge results for further theoretical investigations.

The R-matrix calculation results for the partial cross sections are shown in the upper panel of Figure 5. By examining the partial cross sections into each final, photodetached Ni continuum, the dominant contributions are found from photodetachment into the #1, 2, 4, 5, and 6 final state continua. These channels give rise to the sole giant resonance structure, while there is almost no resonance signal in the final target state symmetries of # 3, 7, 8, 10, 11, 13, 14, 15, and 16 in the $3p \rightarrow 3d$ excitation photon energy region 60 - 70 eV (the upper states are energetically inaccessible, other continua are forbidden by symmetry or selection-rules). Two prominent *s*-wave thresholds appear in the partial cross section for the #9 and #12 final target states. In the middle panel of Figure 5, the total cross section has been broken into its three final symmetries (^{2}P, ^{2}F and ^{2}D), and, as anticipated, the ^{2}P symmetry shows a prominent resonance, while the ^{2}F and ^{2}D symmetries show no resonance signal, indicating that the giant resonance is only of ^{2}P symmetry, consistent with the symmetry of the ($3p^5 3d^{10} 4s^2$ ^{2}P) $3p \rightarrow 3d$ excitation. Furthermore, the autoionizing channels show just *s*-wave on-sets.

C. Discussions

Negative ions for which the valence shell can be filled completely (or become half full) by photoexcitation of an inner-shell electron may exhibit *Feshbach* resonances below the neutral parent state due to the enhanced stabilization. Such effects were observed in the inner-shell photodetachment of He^- [8], S^- [9], O^- [56], Se^- [57], and Te^- [10]. Such stabilization can also occur when a sub-shell is filled by photoexcitation of an inner-shell electron, however this proves to be more difficult to predict. This can be seen in the interesting case of Pt^- [25], where the singly vacant 5*d* shell of Pt^- can be filled by photoexcitation of a 4*f* electron or of a 5*p* electron. The $4f \rightarrow 5d$ excitation produced a very strong, narrow [0.243(2) eV] Feshbach resonance, bound by 2.3 eV below its parent state, as well as a weaker fine-structure resonance, while the $5p \rightarrow 5d$ excitation appeared as a broad shape resonance lying roughly 1 eV about the detachment threshold. This difference in resonance character was qualitatively explained by the very different core-valence interactions from the different core holes, arising largely from the fact the 4*f* orbital is about 20 times smaller than the 5*p* and 5*d* orbitals. It is therefore argued that the much closer proximity of the 5*p* to the 5*d* electrons leads to a stronger interaction, destabilizing the orbital.

In Ni^- ([Ar] $3d^9 4s^2\ ^2D_{5/2}$), a 3*p* electron is being promoted into the 3*d* orbital. One may therefore expect a behavior closer to that of the $5p \rightarrow 5d$ excitation in Pt^-. However, the larger separation of the *p* and *d* orbitals in Ni, as compared to Pt, may allow the resonant state to be more strongly bound in Ni. Indeed, a strong *Feshbach* resonance dominates the measured photodetachment spectrum for Ni^- leading to Ni^+, as seen in Figure 3, and a clear resonance feature is observed in all Ni^+, Ni^{2+}, and Ni^{3+} channels due

to the $3p \rightarrow 3d$ excitation, which is filling the $3d$ shell to form the $3p^5 3d^{10} 4s^2$ (^{2}P) Ni^{-*} state.

NIST database calculations of Ni^+ term energies have determined the energy levels of interest below the Ni^{2+} limit, which are reproduced in Figure 2. The main formation of Ni^+ can be explained through simple Auger decay to Ni^+ $3p^6 3d^9$, Ni^+ $3p^6 3d^8 4s^1$, or Ni^+ $3p^6 3d^7 4s^2$. However, these states lie below the Ni^{2+} ground state, so further autodetachment is not possible. Simultaneous multi-electron photodetachment could lead to the formation of Ni^{2+}. Such a two-electron detachment threshold was observed in the measured Fe^- photodetachment cross section [23], as evidenced by a Wannier threshold law [58] extracted from the difference spectrum. However, we find no evidence of multi-electron threshold detachment in the Ni^- spectra presented here.

For a limited range above single-electron photodetachment threshold, the partial cross section is given by Wigner law [59]: $\sigma(h\nu) = \sigma_0(h\nu - E_{threshold})^{l+1/2}$, where $h\nu$ is the energy of the incoming photon, $E_{threshold}$ is the threshold energy, l is the angular momentum of the free electron (ejected from the negative ion), and σ_0 is a constant. According to dipole selection rules, if a $3p$ electron ($l_0 = 1$) is detached from Ni^-, the photoelectron angular momentum ($l = |l_0 \pm 1|$) can be $l = 0$ (an s-wave) or $l = 2$ (a d-wave).

In the photodetachment cross section, Feshbach resonances give rise to characteristic, often asymmetric structures. The general expression for the photodetachment cross section, $\sigma(h\nu)$, in the vicinity of the autodetaching state embedded in one continuum has been derived by Fano [60], giving the analytic formula:

$$\sigma(h\nu) = \sigma_b(h\nu) + \sigma_a (\varepsilon+q)^2/(\varepsilon^2 + 1) \qquad (1)$$

Here, $\sigma_b(h\nu)$ is the background due to the non-resonant process; σ_a is the resonant part of the total cross section; q is the Fano asymmetry parameter; Γ is the width of the resonance; and ε is the energy detuning from resonance:

$$\varepsilon = (h\nu - E_0)/(\Gamma/2) \qquad (2)$$

where $h\nu$ is the photon energy; and E_0 is the resonance energy.

Figure 6 shows the results for formation of Ni^{n+} (n =1, 2, and 3) from photodetachment of Ni^- near the $3p$ detachment threshold. In order to model the observed structures, a sum of a Fano profile, see Eq. (1), a linear background, and a Wigner s-wave ($l=0$), was fitted to the Ni^+ and Ni^{2+} experimental data. The result of this fit is shown by the solid thick red line in Figure 6. We also tried the fit described above for the Ni^{3+} data, but the poor statistics of the experimental data for Ni^{3+} leads to a very large uncertainty in the Ni^{3+} parameters returned by the fit. Therefore, for the Ni^{3+} experimental data, the solid red curve shown in Figure 6 was obtained by fitting only the amplitude and linear background in the sum, while the line center, width, shape parameter, and threshold position were kept fixed at the values retrieved from the Ni^+ experimental data fit, as reported in Table III and Table IV.

In the photodetachment cross section leading to formation of Ni^+ from Ni^-, the resonance arising from the $3p^6 3d^9 4s^2$ [$^2D_{5/2}$] $\rightarrow$ $3p^5 3d^{10} 4s^2$ [^2P] excitation is observed at 64.926 ± 0.019 eV and the fit returns a width of 1.52 ± 0.02 eV and a line shape parameter of 3.02 ± 0.21. The fit yields a threshold position $E_{threshold}$ = 65.02 ± 0.04 eV for the Wigner s-wave. The quoted total errors listed for the resonance line center and the threshold energy are one-standard deviation (SD) of the photon energy calibration uncertainty added in quadrature with the statistical uncertainties in the fitting parameters

for the threshold and resonance energies. The resonance width and the difference between the resonance energy and threshold energy (Δ) are not sensitive to the photon energy calibration uncertainty.

The Feshbach resonance appears in all Ni^+, Ni^{2+}, and Ni^{3+} detected channels. The energy, width, and shape parameter extracted from the fit are very close for both Ni^+ and Ni^{2+} resonance confirming that the initial photodetachment process is the same, with the products subsequently formed via different Auger decay channels from the same intermediate Ni state. In the theoretical calculations, only the cross section to the ^2P symmetry shows an asymmetric structure – a Fano profile – with calculated resonance energy ε_{theory} = 64.893 eV, and natural width $FWHM_{theory}$ = 1.524 eV. The resonance energy and width were obtained by fitting the R-matrix total cross section with a Fano profile. The energy and width of the resonance predicted by the theory are in good agreement with the measured values shown in Table III. Our crude atomic description of the resonance (using an atomic basis with only 16 of the 3*p*-excited Ni* final targets states and no relativistic effects) led to severe overestimates of the absolute cross section. At a photon energy of 65 eV, the theoretically predicted total cross section is about five times larger than the cross section measured in this experiment, $\sigma_{theory}/\sigma_{experiment}\sim$ 5. If most of the cross section for Ni^- is due to the 3*d* and 4*s* photodetachment to the lowest states, and these states lie below the Ni^+ ground state, no autoionizing process to ionic products is possible, and the large discrepancy between the calculated cross section and measured cross section is due to the fact that the neutral Ni channel is not observed. A similar situation occurred for inner-shell photodetachment of Ru^- negative ion where $\sigma_{theory}/\sigma_{experiment}\sim$ 4 [24].

Due to much poorer statistics, the characteristics of the Feshbach resonance and the threshold position could not be extracted from the Ni^{3+} experimental data. We note, however, that Ni^{3+} signal is observed below 62.1 eV, which is energetically impossible as this lies below the Ni^{3+} grounds state (62.153(19) eV [47]). There is therefore clearly some contamination in this signal channel. Considering the exceedingly small Ni^{3+} signals involved, this is not unexpected. A similar magnitude background was also observed in the similarly weak Pt^{3+} spectrum in a previous experiment in Pt^- [25]. There it was argued that the background likely arose from the presence of small amounts of higher-order light known to be present on this beamline, and may also be responsible for the contamination observed here. We also note that cross-talk with other product channels can be ruled out for a number of reasons. First, the various signal channels appeared to be well separated in the experiment. Second, the product with experimental parameters nearest to the Ni^{3+} signal is Ni^{2+}, but the overall Ni^{3+} signal is very different to that observed for Ni^{2+}, so the latter cannot account for the signal contamination. Third, the strength of the continuum detachment (as measured by the fit Wigner amplitude) relative to the Fano intensity, are very different for each of the channels, as we will discuss presently.

The relative strengths of the resonant detachment channel compared to the continuum detachment channel differ greatly between the three final products. We can estimate this from the amplitudes of the Fano and Wigner profiles obtained from the fit. The signal obtained from the resonance (relative to that from the Wigner-threshold) is found to be 5.8(9) times larger for the Ni^+ product than for Ni^{2+}. For Ni^+ relative to Ni^{3+}, we obtain a factor of about 80 (accurate to only about a factor of 2 due to the much

poorer statistics of in the Ni^{3+} signal). This shows that decay of the resonance greatly prefers the production of smaller charge states as compared to the decay of the direct photodetachment channel.

We therefore believe that the features observed in the Ni^{3+} spectrum of Figure 6 are indeed due to Ni^- to Ni^{3+} photodetachment, on top of an underlying broad background. In such a case, the production of Ni^{3+} from the resonant Ni^- $3p^5 3d^{10} 4s^2$ excitation most likely involves a highly correlated multi-electron (potentially up to 5) decay mechanism, as there are few, if any, intermediate states between the excited Ni^- state and the ground state of Ni^{3+}. The low probability of this decay is reflected in the factor of 2000 to 3000 weaker Ni^{3+} as signal, as compared to Ni^+, from this resonant transition. We note that this mirrors the situation in Pt^- very closely, and similar situation was observed in S^- [9] where simultaneous multi-Auger processes are required to explain the formation of S^{2+} and S^{3+} near the threshold.

Finally, the rapid rise in Ni^{3+} signal beginning at about 75 eV is, no doubt, from the opening of a new photodetachment channel. A Wigner *s*-wave + *d*-wave threshold law produces a very faithful fit to these data with a threshold around 76.2 eV (see Figure 7), and strongly suggests single-electron photodetachment to a core-excited Ni state with subsequent multi-Auger decay to the Ni^{3+} ground state. This second step must again involve a highly correlated multi-Auger decay transition involving up to a total of 4 electrons. We performed separate multiconfigurational Hartree-Fock (MCHF) calculations which located the $3p^5 3d^9 4s^2$ Ni core-excited state energy at 77.06 eV.

D. Comparison of Ni^- and Fe^- inner-shell photodetachment

Recently, we investigated the photodetachment cross section of Fe^- (Z = 26) in the 48-to-72 eV photon energy range [23]. Despite the similar electronic configuration of Ni^- ([Ar] $3d^9 4s^2\ ^2D_{5/2}$) and Fe^- ([Ar] $3d^7 4s^2\ ^4F_{9/2}$), the behavior of their photodetachment cross section in the $3p \rightarrow 3d$ excitation region is strikingly different.

As discussed above, excitation of a $3p$ electron in Ni^- leads to the $3p^5 3d^{10} 4s^2$ [^{2}P] state situated just *below* the correspondent $3p^5 3d^9 4s^2$ state in the Ni neutral parent atom, as shown in Figure 8. The final state produced by the inner-shell excitation $3p \rightarrow 3d$ has enhanced stability due to the additional binding energy of the full $3d$ valence shell. A strong Feshbach resonance describes the Ni^- photodetachment spectrum very well, and the sum of Fano profile, Wigner s-wave (l=0), and linear background provides an excellent fit for the Ni^- experimental data, as shown in Figure 6.

In contrast, excitation of a $3p$ electron in Fe^- leads to a quasi-discrete $3p^5 3d^8 4s^2$ [^{4}D, ^{4}F, ^{4}G] state situated just *above* the corresponding $3p^5 3d^7 4s^2$ state in the Fe neutral atom, as shown in Figure 8. Thus, the photodetachment cross section for Fe^- is dominated by three large, well-separated *shape* resonances.

Since the $3p \rightarrow 3d$ excitation in Fe^- was just *above* the $3p$ ionization threshold it can thus decay to its own continuum, however in Ni^-, the $3p \rightarrow 3d$ excitation is just *below* the $3p$ ionization threshold, thus it can only decay to other lower continua and the full Fano mechanism is observable. Consequently, there is a change from a broad shape resonance $3p \rightarrow 3d$, above $3p$ threshold in Fe^- to a much narrower $3p \rightarrow 3d$ Feshbach resonance, below $3p$ threshold in Ni^-.

The Fe^- → Fe^+ total photodetachment cross section exhibits three shape resonances in the region of 50 - 56 eV but otherwise is flat with a magnitude of the order 1 Mb below 50 eV increasing to 2 Mb at 70 eV. The Ni^- → Ni^+ total photodetachment cross section exhibits one Feshbach resonance at 64.9 eV, with a relatively flat cross section of the order 1.2 Mb below 60 eV increasing to 2.1 Mb at 90 eV. The background below the 3*p* threshold region is due to the 4*s* and especially 3*d* absorption. Studying the absolute photoionization cross section of Ca^+ - Ni^+ ions, Hansen *et al.* [38] found that the 3*d* absorption continues as a background in the 3*p* region, and the 3*d* cross section is roughly proportional with the number of 3*d* electrons in the respective ground state. The ratio of the background cross section below threshold to the maximum cross section of the resonance peak increases from 16.7% in Fe^- (7 electrons in the 3*d* orbital) to 38.1% in Ni^- (9 electrons in the 3*d* orbital).

On the other hand, the maximum peak cross section decreases from about 6 Mb in Fe^- → Fe^+ [23] to about 2 Mb in Ni^-→Ni^+. Also, in the doubly charged product channel, the maximum peak cross section decreases from about 0.6 Mb in Fe^- → Fe^{2+} [23] to about 0.2 Mb in Ni^-→Ni^{2+}. The decreasing peak cross section was also observed for the photoionization of the singly positive charged ions in the sequence Ca^+ to Ni^+, and can be explained by the filling of the 3*d* shell that reduces the number of final states accessible [38]. The ratio of the maximum photodetachment cross section for singly- to doubly-charged products is about the same for both Ni^- and Fe^- negative ions, $\sigma_{Ni+}/\sigma_{Ni2+} \approx \sigma_{Fe+}/\sigma_{Fe2+} \approx 10$.

4. Summary

We have reported absolutely-scaled inner-shell photodetachment cross section data for the Ni^- negative ion near and above the 3*p* detachment threshold, in the photon energy range 60 - 90 eV. In the inner-shell photodetachment of Ni^-, the strong $3p \rightarrow 3d$ photoexcitation manifests itself as a Feshbach resonance below the *3p* threshold, providing an interesting contrast to our previous observation of Fe^- inner-shell photodetachment, where the similar excited state lies just above the detachment threshold, leading to a shape resonance in the 3*p* photodetachment continuum. Furthermore, the absolute photodetachment cross sections for Ni^- leading to Ni^+, and the ratio of channel strengths (Ni^{2+}/Ni^+) and (Ni^{3+}/Ni^+), were measured at four photon energies, providing reference data for astrophysics and plasma physics.

Acknowledgements

This work was supported by DoE, Office of Science, BES, Chemical, Geoscience and Biological Divisions under contract No. DE-SC0012376; DE-FG02-86ER13491 (D.R.). The ALS is funded by DoE, Scientific User Facilities Division. N. D. Gibson and C. W. Walter acknowledge support from NSF Grant Nos. 1068308 and 1404109.

References

[1] T. Andersen, Phys. Rep. **394**, 157 (2004).

[2] C. W. Walter, N. D. Gibson, Y. –Gi Li, D. J. Matyas, R. M. Alton, S. E. Lou, R. L. Field II, D. Hanstorp, Li Pan, and D. R. Beck, Phys. Rev. A **84**, 032514 (2011).

[3] C. W. Walter, N. D. Gibson, D. J. Matyas, C. Crocker, K. A. Dungan, B. R. Matola, and J. Rohlen, Phys. Rev. Lett. **113**, 063001 (2014).

[4] R. C. Bilodeau and H. K. Haugen, Phys. Rev. Lett. **85**, 534 (2000).

[5] D. G. Leopold and W. C. Lineberger, J. Chem. Phys. **85**, 51 (1986).

[6] T. Andersen, H. K. Haugen, H. Hotop, J. Phys. Chem. Ref. Data **28**, 1511 (1999).

[7] S. J. Buckman, C. W. Clark, Rev. Mod. Phys. **66**, 539 (1994).

[8] R. C. Bilodeau, J. D. Bozek, A. Aguilar, G. D. Ackerman, G. Turri, and N. Berrah, Phys. Rev. Lett. **93**, 193001 (2004).

[9] R. C. Bilodeau, N. D. Gibson, J. D. Bozek, C. W. Walter, G. D. Ackerman, P. Andersen,J. G. Heredia, M. Perri, and N. Berrah, Phys. Rev. A **72**, 050701(R) (2005).

[10] H. Kjeldsen, F. Folkmann, T. S. Jacobsen, and J. B. West, Phys. Rev. A **69**, 050501(R) (2004).

[11] J. R. Peterson, Y. K. Bae, and D. L. Huestis, Phys. Rev. Lett. **55**, 692 (1985).

[12] Y. K. Bae and J. R. Peterson, Phys. Rev. A **32**, 1917 (1985).

[13] T. W. Gorczyca, O. Zatsarinny, H. –L. Zhou, S. T. Manson, Z. Felfli, and A. Z. Msezane, Phys. Rev. A **68**, 050703 (R) (2003).

[14] H. Kjeldsen, P. Andersen, F. Folkmann, B. Kristensen, and T. J. Andersen, J. Phys. B **34**, L353 (2001).

[15] N. Berrah, J. D. Bozek, A. A. Wills, G. Turri, H. -L. Zhou, S. T. Manson, G. Ackerman, B. Rude, N. D. Gibson, C. W. Walter, L. Vo Ky, A. Hibbert, and S. M. Ferguson, Phys. Rev. Lett **87**, 253002 (2001).

[16] H.–L. Zhou, S. T. Manson, L.Vo Ky, N. Feautrier, and A. Hibbert, Phys. Rev. Lett. **87**, 023001 (2001).

[17] N. Berrah, R. C. Bilodeau, I. Dumitriu, J. D. Bozek, N. D. Gibson, C. W. Walter, G. D. Ackerman, O. Zatsarinny, and T. W. Gorczyca, Phys. Rev. A **76**, 032713 (2007).

[18] T. W. Gorczyca, Radiat. Phys. Chem. **70**, 407 (2004).

[19] N. Berrah, R. C. Bilodeau, G. D. Ackerman, J. D. Bozek, G. Turri, E. Kukk, W. T. Cheng, and G. Snell, Radiat. Phys. Chem. **70**, 491 (2004).

[20] C. W. Walter, N. D. Gibson, R. C. Bilodeau, N.Berrah, J. D. Bozek, G. D. Ackerman, and A. Aguilar, Phys. Rev. A **73**, 062702 (2006).

[21] N. D. Gibson, C. W. Walter, O. Zatsariny, T. W. Gorczyca, G. D. Ackerman, J. D. Bozek, M. Martins, B. M. McLaughlin, and N. Berrah, Phys. Rev. A **67**, 030703 (R) (2003).

[22] G. Y. Kashenock and V. K. Ivanov, J. Phys. B **39**, 1379 (2006).

[23] I. Dumitriu, R. C. Bilodeau, T. W. Gorczyca, C. W. Walter, N. D. Gibson, A. Aguilar, Z. Pesic, D. Rolles, and N. Berrah, Phys. Rev. A **81**, 053404 (2010).

[24] I. Dumitriu, R. C. Bilodeau, T. W. Gorczyca, C. W. Walter, N. D. Gibson, Z. D. Pesic, D. Rolles, and N. Berrah, Phys. Rev. A **82**, 043434 (2010).

[25] R. C. Bilodeau, I. Dumitriu, D. Rolles, C. W. Walter, N. D. Gibson, and N. Berrah, Phys. Rev. A **80**,031403 (2009).

[26] M. Martins, K. Godehusen, T. Richter, P. Wernet and P. Zimmermann, J. Phys. B **39**, R79 (2006).

[27] S. B. Whitfield, R. Wehlitz, and M. Martins, Rad. Phys. Chem. **70**, 3 (2004).

[28] B. Sonntag and P. Zimmermann, Rep. Prog. Phys. **55**, 911 (1992).

[29] K. J. Ross and B. Sonntag, Rev. Sci. Intrum. **66**, 4409 (1995).

[30] H. Aksela, S. Aksela, T. Pekkala, and M. Wallenius, Phys. Rev. A **35**, 1522 (1987).

[31] M. Magnuson, N. Wassdahl, A. Nilsson, A. Föhlich, J. Nordgren, and N. Mårtensson, Phys. Rev. B **58**, 3677 (1998).

[32] E. Schmidt, H. Schröder, B. Sonntag, H. Voss, and H. E. Wetzel, J. Phys. B **17**, 707 (1984).

[33] K. Tiedtke, Ch. Gerth, B. Kanngießer, B. Obst, and P. Zimmermann, Phys. Rev. A **60**, 3008 (1999).

[34] K. Godehusen, and H. E. Wetzel, J. Phys. B **16**, 2961 (1983).

[35] E. Schmidt, T. Richter, and P. Zimmermann, Phys. Rev. Lett. **88**, 217601 (2002).

[36] H. Feist, M. Feldt, Ch. Gerth, M. Martins, P. Sladeczek, and P. Zimmermann, Phys. Rev. A **53**, 760 (1996).

[37] A. Verweyen, A. von dem Borne, P. Glatzel, Ph. Wernet, B. Sonntag, K. Godehusen, Ch. Gerth, and P. Zimmermann, Phys. Rev. A **60**, 737 (1999).

[38] J. E. Hansen, H. Kjeldsen, F. Folkmann, M. Martins, and J. B. West, J. Phys. B **40**, 293 (2007).

[39] M. Scheer, C. A. Brodie, R. C. Bilodeau, and H. K. Haugen, Phys. Rev. A **58**, 2051 (1998).

[40] Z. Cai and D. R. Beck, Phys. Rev. A **40**, 1657 (1989).

[41] M. Kaminska, V. T. Davis, O. M. Hole,R. F. Nascimento, K. C. Chartkunchand, M. Blom, M. Björkhage, A. Källberg, P. Löfgren, P. Reinhed, S. Rosen, A. Simonsson, R. D. Thomas, S. Mannervik, P. A. Neill, J. S. Thompson, H. T. Schmidt, H. Cederquist, and D. Hanstorp, Phys. Rev. A **93**, 012512 (2016).

[42] A. Müller, Phys. Scr. **90**, 054004 (2015).

[43] A.M. Covington, A. Aguilar, I. R. Covington, M. F. Gharaibeh, G. Hinojosa, C. A. Shirley, R. A. Phaneuf, I. Alvarez, C. Cisneros, I. Dominguez-Lopez, M. M. Sant'Anna, A. S. Schlachter, B. M. McLaughlin, and A. Dalgarno, Phys. Rev. A **66**, 062710 (2002).

[44] R. Middleton, *A Negative Ion Cookbook*, Dept. of Physics, University of Pennsylvania, Philadelphia, PA, 1990.

[45] Kessler, K. Brück, C. Baktash, J. R. Beene, Ch. Geppert, C. C. Havener, H. F. Kraus e, Y. Liu, D. R. Schultz,D. W. Stracener, C. R. Vane, and K. Wendt, J. Phys. B **40**, 4413–4432 (2007). *NIST Atomic Spectra Database* (ver. 5.2), http://physics.nist.gov/asd

[46] J. Sugar and C. Corliss, J. Phys. Chem. Ref. Data **14**, Suppl. 2, 1–664 (1985). *NIST Atomic Spectra Database* (ver. 5.2), http://physics.nist.gov/asd

[47] O. Garcia-Riquelme and F. R. Rico, Phys. Scr. **45**, 212–230 (1992). *NIST Atomic Spectra Database* (ver. 5.2), http://physics.nist.gov/asd

[48] W. Lotz, J. Opt. Soc. Am. **57**, 873–878 (1967). *NIST Atomic Spectra Database* (ver. 5.2), http://physics.nist.gov/asd

[49] F. Combet Farnoux and M. Ben Amar, Phys. Rev. A **21**, 1975 (1980).

[50] M. Domke, K. Schulz, G. Remmers, and G. Kainde, Phys. Rev. A **53**, 1424 (1996).

[51] http://www.sisweb.com/simion.htm

[52] R. C. Bilodeau, J. D. Bozek, N. D. Gibson, C. W. Walter, G. D. Ackerman, I. Dumitriu, and N. Berrah, Phys. Rev. Lett. **95**, 083001 (2005).

[53] J. C. Fuggle and N. Mårtensson, J. Electron Spectrosc. Relat. Phenom. **21**, 275 (1980); httpl://xdb.lbl.gov

[54] P. G. Burke and K. A. Berrington, *Atomic and Molecular Processes: An R-Matrix Approach* (IOP Publishing, Bristol, 1993).

[55] K. A. Berrington, W. B. Eissner, and P. N. Norrington, Comput. Phys. Commun. **92**, 290 (1995).

[56] N. D. Gibson, R. C. Bilodeau, C. W. Walter, D. Hanstorp, A. Aguilar, N. Berrah, D. J. Matyas, Y. -G. Li, R. M. Alton, S. E. Lou, XXVII Inter. Conf. Phot. Elect. Atom. Coll., Belfast, Northern Ireland, Th 159 (2011).

[57] N. D. Gibson, C. W. Walter, R. L. Field III, D. J. Carman, J. Z. Shapiro, R. C. Bilodeau, I. Dumitriu, N. Berrah, A. Aguilar, XXVI Inter. Conf. Phot. Elect. Atom. Coll., Kalamazoo, MI, Th 159 (2009).

[58] G. H. Wannier, Phys. Rev. **90**, 817 (1953).

[59] E. P. Wigner, Phys. Rev. **73**, 1002 (1948).

[60] U. Fano, Phys. Rev. **124**, 1866 (1961).

Figure Caption:

FIG. 1. (color online) Schematic of the ALS ion-photon beam (IPB) endstation at beamline 10.0.1.

FIG. 2. (color online) Simplified energy level diagram for Ni^- and the relevant states in the parent Ni atom and positive ions Ni^+, Ni^{2+}, and Ni^{3+}. For clarity, the diagram is not to scale. The electron affinity of atomic Ni, 1.15716(12) eV [39], and all other energies are reported relative to the Ni^- ground state. The dotted lines represent the ground states of Ni [39], Ni^+ [45], Ni^{2+} [46], and Ni^{3+} [47]. The grey bands indicate the available continua. Interference between direct photodetachment of an electron from Ni^- and $3p \rightarrow 3d$ excitation followed by autodetachment is indicated by arrows.

FIG. 3. (color online) The measured photodetachment cross section for Ni^+, Ni^{2+} and Ni^{3+} from Ni^-. The cross-section scale was established by making absolute measurements for $\sigma(Ni^+)$ (denoted by filled circles) at the three energies shown.

FIG. 4. (color online) (upper panel) Theoretical results are shown for the total cross section calculated in length (dashed curve) and velocity (solid curve) gauge. (lower panel) The theoretical total cross section calculated in length gauge was shifted by - 4.8 Mb in order to overlap the theoretical total cross section calculated in velocity gauge.

FIG. 5. (color online) (upper panel) The partial cross sections are shown for the all 16 target final states listed in Table II. (middle panel) A partitioning of the photodetachment

cross section into the ^{2}P (solid green line),^{2}F (dashed-dot-dot blue line), ^{2}D (dashed cyan line), and autoionizing (solid purple) channel contributions. (lower panel) The measured cross section of Ni^+ ions following photodetachment of Ni^- over 60 - 90 eV photon energy range. The blue open circles are the experimental data.

FIG. 6. (color online) The measured photodetachment cross section of Ni^+, Ni^{2+}, and Ni^{3+} following photodetachment of Ni^- over the resonance photon energy range. The open circles are the experimental data. For Ni^+ and Ni^{2+}, the solid line is the sum of a Fano profile with a linear background and a Wigner *s* –wave (l=0) fit to the data. Note: the range of the fit, 60 eV to 68 eV, is indicated by the solid line, and the dashed line shows extension beyond fit range. The long dashed line is the Wigner s-wave (l=0) contribution to the fit to the data. The dash-dot-dot-dot line indicates the Fano profile contribution to the fit. The dash-dot line shows the linear background contribution to the fit. See text for details on Ni^{3+} experimental data fit.

FIG. 7. (color online) The measured photodetachment cross section of Ni^{3+} following photodetachment of Ni^-. The open circles are the experimental data. The solid line is the sum of a Wigner *s*–wave (l=0) and Wigner *d* –wave (l=2) fit to the data. Note: the range of the fit, 72 eV to 83 eV, is indicated by the solid line, and the dashed line shows extension beyond fit range.

FIG. 8. (color online) Simplified energy-level diagram for the Ni^- and Fe^- ions, along with the relevant states in the parent atom and positive ions reported relative to the

ground state of the negative ion. For clarity purpose, the diagram is not to scale. The solid lines represent the measured state energies. The dotted lines represent the ground state for neutral atoms and the positive ions. The dashed lines are the theoretically calculated energies of 3*p* excited states in neutral atoms. Interference between direct emission of an electron from Ni^- negative ion into the continuum and $3p \rightarrow 3d$ excitation followed by autodetachment, as indicated by arrows, gives rise to a Feshbach resonance. In contrast, excitation of a 3*p* electron in Fe^- leads to shape resonances [23].

TABLE I. Measured absolute cross section $Ni^- \rightarrow Ni^+$ and ratio of channel strengths (Ni^{2+}/Ni^+) and (Ni^{3+}/Ni^+) reported to 1 SD.

TABLE II. Computed energies of excited Ni* final target states.

TABLE III. Characteristics of Feshbach resonances obtained from fitting a sum of a Fano profile, a Wigner *s*-wave (l=0), and a linear background to measured absolute cross section $Ni^- \rightarrow Ni^+$ and Ni^{2+}.

TABLE IV. Threshold obtained from fitting a sum of a Fano profile, a Wigner *s*-wave (l=0), and a linear background to measured absolute cross section $Ni^- \rightarrow Ni^+$ and Ni^{2+}.

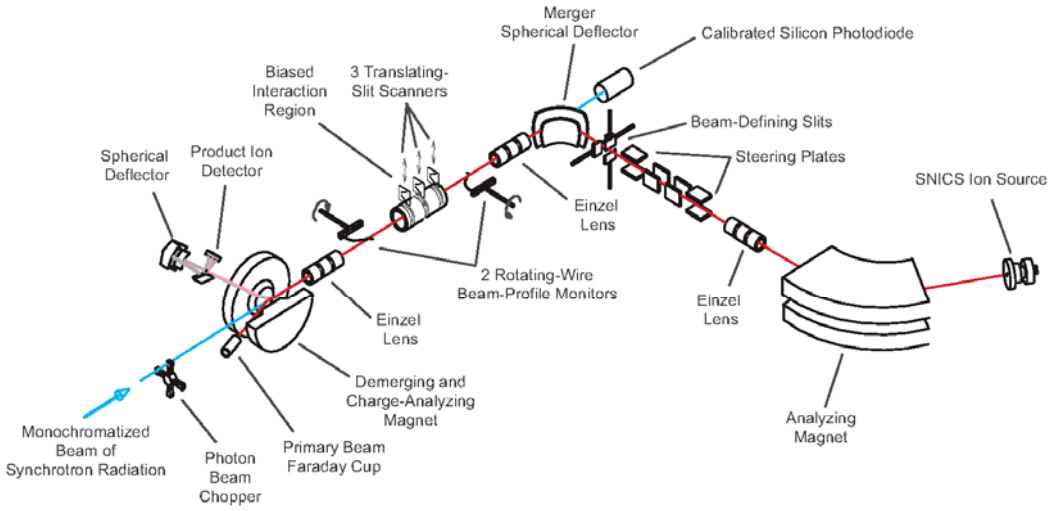
Merger
Spherical Deflector
Calibrated Silicon Photodiode
Biased
Interaction
Region
3 Translating-
Slit Scanners
Beam-Defining Slits
Steering Plates
Spherical
Deflector
Product Ion
Detector
SNICS Ion Source
Einzel
Lens
2 Rotating-Wire
Beam-Profile Monitors
Einzel
Lens
Einzel
Lens
Demerging and
Charge-Analyzing
Magnet
Analyzing
Magnet
Monochromatized
Beam of
Synchrotron Radiation
Photon
Beam
Chopper
Primary Beam
Faraday Cup

FIG. 1.

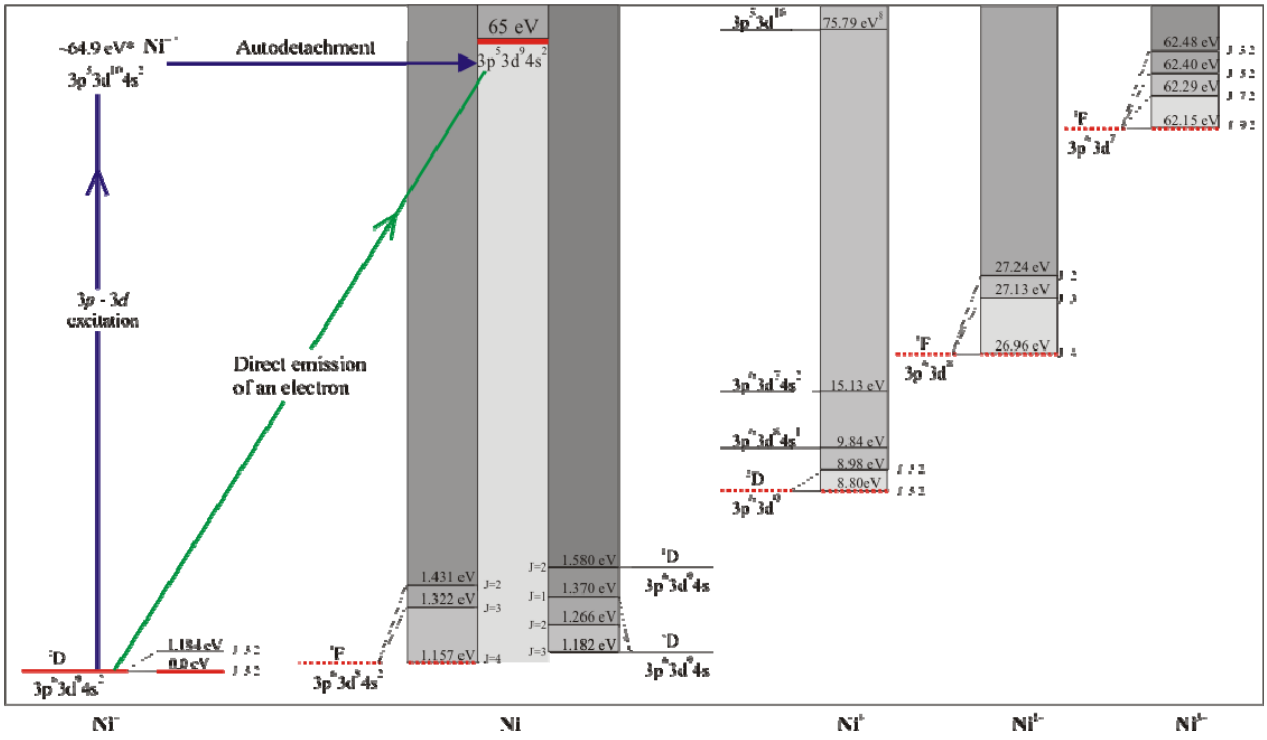

* State energies measured in the present experiment
§ Theoretical predicted energy for this state [49]

FIG. 2.

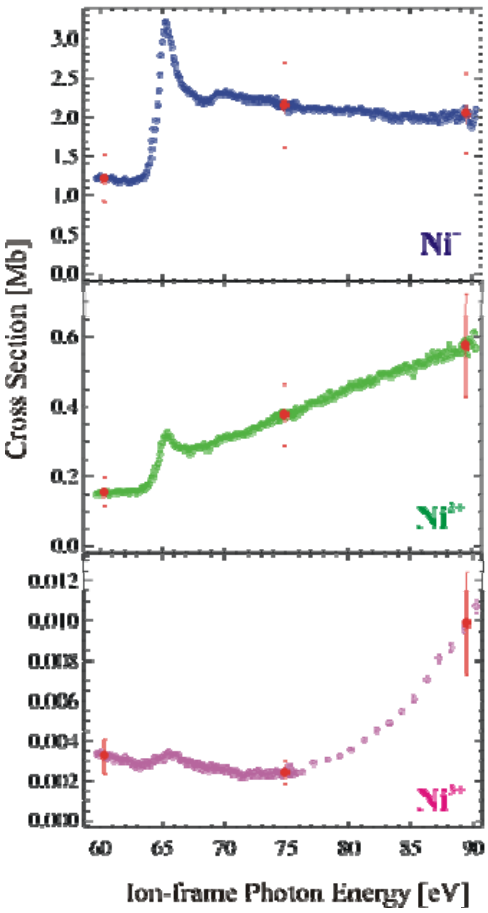

FIG. 3.

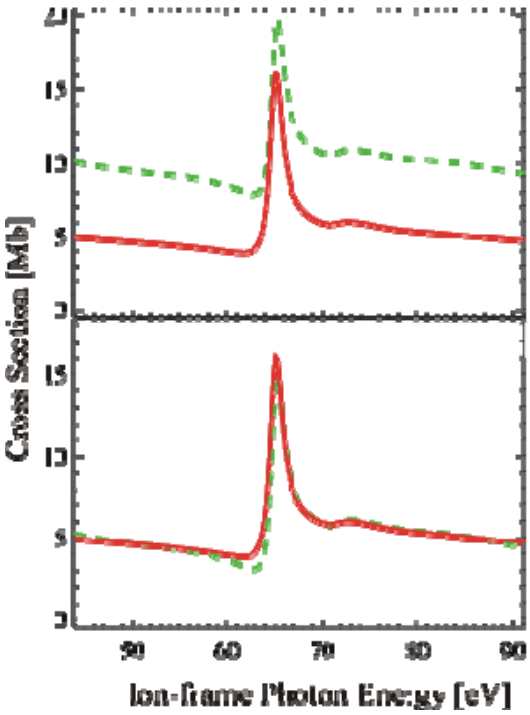

FIG. 4.

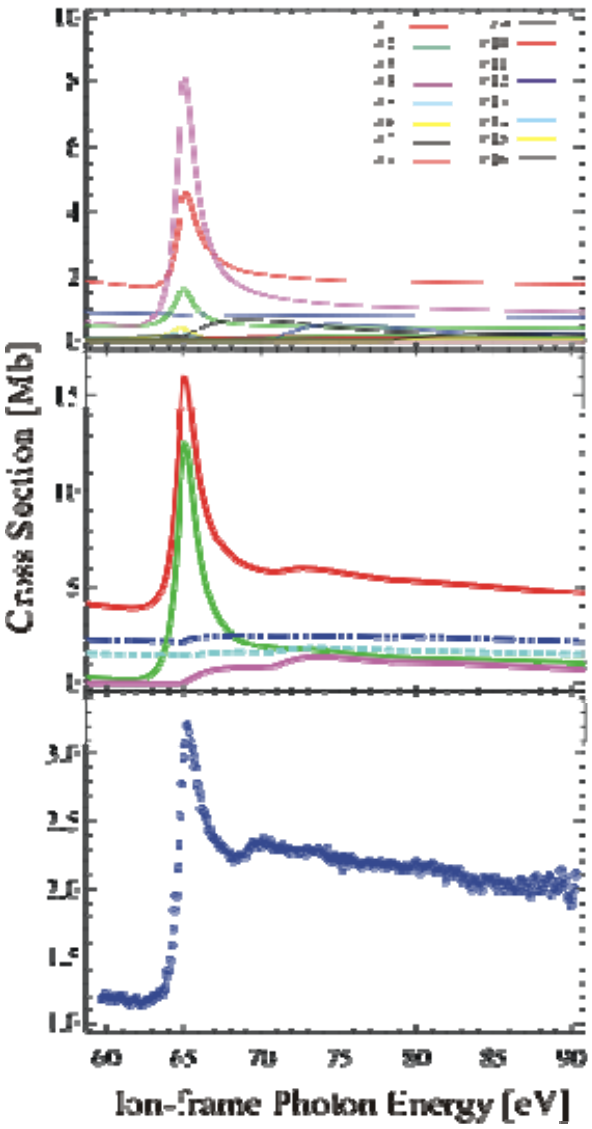
Cross Section [Mb]
60
65
70
75
80
85
90
Ion-Frame Photon Energy [eV]

FIG. 5.

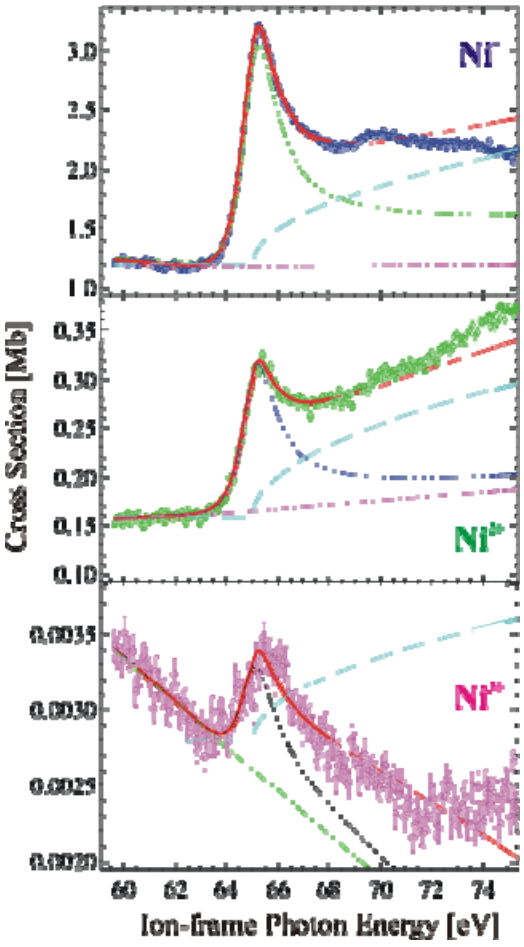

FIG. 6.

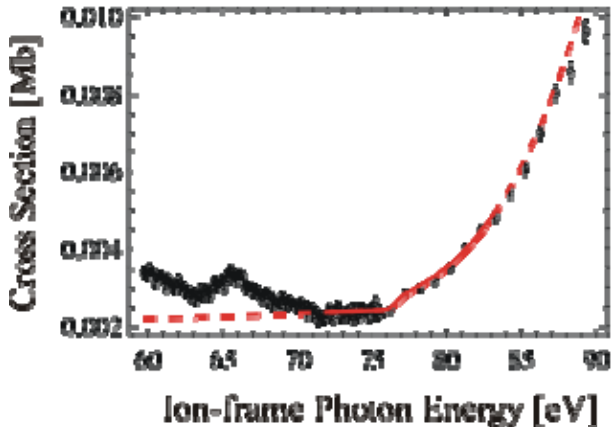
Cross Section [Mb]
0.010
0.0228
0.0226
0.0224
0.0222
60
65
70
75
80
85
90
Ion-frame Photon Energy [eV]

FIG. 7.

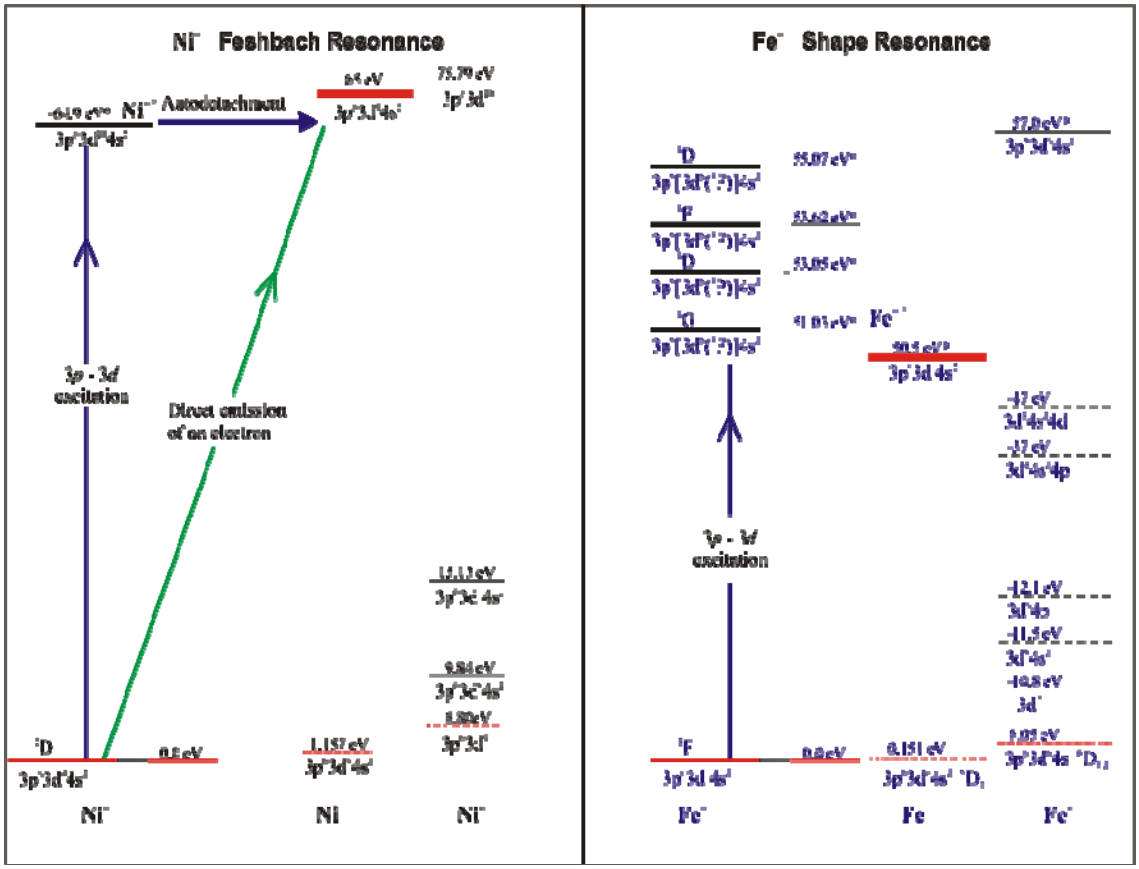

* State energies measured in the present Ni^- and previous Fe^- [23] experiment.

FIG. 8.

TABLE I

Photon Energy [eV]	Cross Section Ni^+ [Mb]	Ratio of the channel strengths Ni^{2+}/Ni^+	Ratio of the channel strengths Ni^{3+}/Ni^+
45.796 ± 0.025	1.15 ± 0.29	0.084 ± 0.007	0.0029 ± 0.0007
60.341 ± 0.015	1.2 ± 0.3	0.130 ± 0.010	0.0027 ± 0.0003
74.887 ± 0.025	2.2 ± 0.5	0.171 ± 0.012	0.0011 ± 0.0001
89.43 ± 0.08	2.1 ± 0.5	0.280 ± 0.019	0.0047 ± 0.0005

TABLE II

Target	Configuration	LS Term	Calculated Threshold Energy Relative to ground-state Ni [eV]
#1	$3p^6 3d^8 4s^2$	^{3}F	0.00
#2	$3p^6 3d^8 4s^2$	^{1}D	1.99
#3	$3p^6 3d^8 4s^2$	^{3}P	2.42
#4	$3p^6 3d^8 4s^2$	^{1}G	3.12
#5	$3p^6 3d^9 4s$	^{3}D	5.39
#6	$3p^6 3d^9 4s$	^{1}D	5.76
#7	$3p^6 3d^8 4s^2$	^{1}S	7.69
#8	$3p^6 3d^{10}$	^{1}S	22.50
#9	$3p^5 3d^9 4s^2$	^{1}F	66.07
#10	$3p^5 3d^9 4s^2$	^{1}D	66.93
#11	$3p^5 3d^9 4s^2$	^{3}P	71.02
#12	$3p^5 3d^9 4s^2$	^{3}D	71.86
#13	$3p^5 3d^{10} 4s$	^{3}P	73.36
#14	$3p^5 3d^{10} 4s$	^{1}P	73.55
#15	$3p^5 3d^9 4s^2$	^{1}P	78.59
#16	$3p^5 3d^9 4s^2$	^{1}F	79.62

TABLE III

Photodetachment of Ni^- leading to	Resonance Energy [eV]	Width [eV]	Shape Parameter q
Ni^+	64.926±0.019	1.52±0.02	3.02 ± 0.21
Ni^{2+}	64.93±0.03	1.50±0.05	3.7 ± 0.8

TABLE IV

Photodetachment of Ni^- leading to	Threshold [eV]	Δ = Threshold - Resonance Energy [eV]
Ni^+	65.02 ± 0.04	0.09 ± 0.04
Ni^{2+}	65.00 ± 0.05	0.08 ± 0.06